Analysis of Grid-forming/following STATCOMs and Synchronous Compensators for Grid-following IBRs stability

Jorge Suárez-Porras, Fidel Fernández-Bernal, Luis Rouco, Régulo E. Ávila-Martínez, Andrés Tomás-Martín, Aurelio García-Cerrada and Emilio José Bueno Peña

***Abstract*—This paper investigates how different compensating devices can enhance the small-signal stability of the system by means of the phase-locked loop (PLL) in inverter-based resources (IBRs) operating in grid-following mode. Three technologies are compared: synchronous compensator (SC), STATCOM operated in grid-forming (GFr) mode, and static synchronous compensator (STATCOM) operated in grid-following (GFl) mode. A systematic control design procedure is proposed for the GFr STATCOM, combining pole-placement for the inner current loop and phase margin design for the outer voltage loop. The study relies on small-signal eigenvalue analysis and time-domain simulations under transient disturbances. To provide a representative case study, a doubly-fed induction generator (DFIG) is used as the IBR device model due to its complex dynamics and direct coupling between the machine and the grid. Results confirm that both SC and GFr STATCOM significantly improve the system stability, whereas GFl STATCOM provides negligible benefits.**

***Index Terms*—Synchronous compensator, synchronous condenser, short-circuit ratio, grid-forming, grid-following, doubly-fed induction generator, reactive power, inverter-based resources, PLL stability.**

I. Introduction

THE increasing penetration of renewable energy sources (RESs) is reshaping modern power systems worldwide. RESs are typically connected through inverter-based resources (IBRs) devices, which inherently lack essential grid-supporting features such as physical inertia and high short-circuit current capability [1]. While synthetic inertia can be emulated through advanced control strategies and energy storage [2], the absence of rotating mass and limited overcurrent capacity impose significant challenges for system operators, particularly as synchronous generation is progressively displaced by IBRs.

To mitigate stability issues under low short-circuit ratio (SCR) conditions, several technologies have been proposed. Among them, synchronous compensators (SCs) [3], [4] and grid-forming (GFr) converters [5], [6] have gained significant attention due to their capability to support voltage and frequency in the grid [7]. SCs provide natural inertia through their rotating mass [8], contributing to frequency stability by limiting the rate of change of frequency (RoCoF). In addition, SCs supply high fault currents, which effectively increase the SCR and improve small-signal stability. However, SCs require a grid-supplied frequency reference to maintain synchronism and, in the absence of a prime mover, they cannot operate in islanded mode.

In contrast, GFr converters can directly impose both voltage and frequency at their terminals. When equipped with sufficient DC-side energy storage, they can provide synthetic inertia via control strategies such as the virtual synchronous machine (VSM) [2]. One of their key advantages is the ability to operate in islanded conditions [9]. Nevertheless, as power electronic devices, their fault current contribution is limited, meaning that GFrs converters do not significantly improve the classical SCR [10]. Despite this, recent studies suggest that GFrs converters can still enhance the small-signal stability of IBR-based systems [6], [11].

The interaction between low-inertia systems and stabilizing technologies has been widely studied. Previous works have shown that instabilities in GFl-IBRs under weak-grid conditions often originate from the instability due to phase-locked loop (PLL) dynamics [12]–[15]. In this paper, we define 'PLL stability' as the condition where the system's stability (or instability) is primarily driven by the PLL dynamics. SCs have been demonstrated to improve PLL stability by reducing the equivalent impedance seen by the converter, effectively increasing the SCR and enhancing stability [3], [16], [17]. On the other hand, GFrs converters can increase small-signal stability by imposing strong voltage references. However, systematic guidelines for tuning the voltage and current control loops of GFrs converters are lacking, and the parameter selection remains a challenging task.

Several works have compared SCs and GFrs converters in terms of cost, operational priorities, and dynamic performance [18], [19]. However, none of the aforementioned studies provides detailed guidelines on how to tune the control parameters of GFr converters in order to explicitly enhance PLL stability in GFl-IBRs. Existing approaches for controller design include pole-placement [20] and virtual impedance-based strategies [21], but to the best of the authors knowledge, no prior work has investigated the tuning of the voltage

This work is part of the Project PID2021-125628OB-C21 funded by MICIU/AEI/10.13039/501100011033 and by ERDF/EU and the grant PRE2022-101606 funded by MICIU/AEI/10.13039/501100011033 and by ESF+. The simulation and analysis in this work have been carried out with a tool partially financed by the project TED2021-130610B-C22, funded by MCIN/AEI/10.13039/501100011033, and by the European Union NextGenerationEU/PRTR.

Jorge Suárez-Porras, Fidel Fernández-Bernal, Régulo E. Ávila-Martínez, Luis Rouco, Andrés Tomás-Martín and Aurelio García-Cerrada are with IIT, ETSI ICAI, Universidad Pontificia Comillas, 28015 Madrid, Spain.

Emilio José Bueno Peña is with UAH - Universidad de Alcalá de Henares, 28801 Alcal de Henares, Madrid, Spain.

Digital Object Identifier XXXXXXXXXXXXXXXXX

control loop of a GFr converter using phase margin design, nor analyzed its impact on the PLL stability of a connected GFr-IBR.

In this work, a comprehensive comparison is carried out between GFr STATCOMs, SCs, and GFl STATCOMs in terms of their ability to enhance the small-signal stability of the PLL in GFl-IBRs. As GFl-IBR, a doubly fed induction generator (DFIG) is used due to its inherent complexity. Both small-signal analysis and time-domain simulations are presented to validate the results.

The main contributions of this paper are:

- It is demonstrated that, contrary to the conventional understanding, a STATCOM operating in grid-forming mode can enhance PLL stability of GFl converters, even though it does not increase the SCR as SCs do due to converter limited over-current capability.
- A systematic control design methodology for GFr converters is proposed, consisting of phase margin-based tuning for the voltage loop and pole-placement design for the current loop. The effect of the phase margin for a given SCR is analyzed.

The rest of the paper is organized as follows. Section II describes the system modeling, including the grid-forming STATCOM, its inner and outer control loops, and the reference models for the DFIG and the synchronous compensator. Section III analyzes by eigenvalue analysis the small-signal stability of the DFIG PLL under three cases: DFIG alone, DFIG with a SC, DFIG with a GFr STATCOM, and DFIG with a GFl STATCOM. Section IV presents time-domain simulations to complement the eigenvalue analysis. Section V concludes the paper. Finally, the appendices provide detailed electromagnetic and electromechanical equations for the DFIG and the SC models.

II. System Modelling

As shown in Fig. 1, the case study of this paper, an IBR is connected to an infinite grid through a transmission line, resulting in a given SCR [22]. The IBR considered in this study is a DFIG, chosen because it represents one of the most complex IBR models. Unlike full converter-based machines, in the DFIG the dynamics of the asynchronous machine remains directly coupled to the PLL, since the stator is connected to the grid and the DC bus does not provide full decoupling between the machine and the network.

Previous studies have shown that in weak grids the main source of instability in IBRs is often associated with the PLL used for synchronization [14], [15], [23]. Since the DFIG is operated in grid-following mode, it relies on a PLL, and therefore becomes vulnerable to instability under such weak-grid conditions.

To enhance the stability of the DFIG PLL, either a SC or a STATCOM in GFr or GFl mode is connected at the point of common coupling (PCC).

The DFIG model corresponds to a 2 MW wind turbine described in [24], while the PLL implementation is shown in Fig. 2. Model parameters are provided in Appendix A.

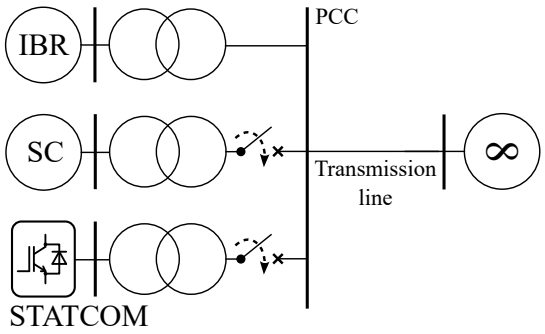


Fig. 1. One-line diagram of the system under study: an IBR connected to the grid through a transmission line, with either an SC or a STATCOM connected to the PCC.

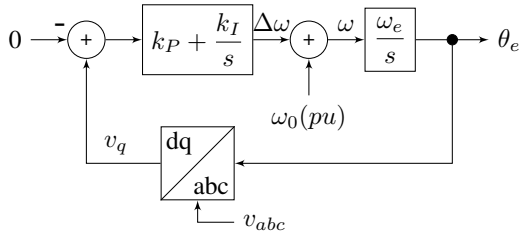


Fig. 2. Phase-locked loop block diagram used in this work.

The SC is modeled as a full synchronous machine connected through a 10% impedance transformer, with data taken from a commercial unit [25] (see Appendix B).

A. Grid-forming STATCOM model

Figure 3 illustrates the STATCOM connected at the PCC. The complete control diagram is shown in Fig. 4. The converter is controlled in GFr mode, regulating its terminal voltage magnitude and frequency to $v_o = 1$ pu and $f = 50$ Hz. The VSM control scheme, adapted from [2], assumes a sufficiently large DC-link capacitor to sustain GFr operation.

As shown in Fig. 4, the reference of active power is subtracted from the measured active power of the converter. Since the STATCOM is not intended to inject active power in steady state (as there is no primary energy source), this reference is typically set to zero. The resulting power imbalance is then processed by the transfer function representing the swing equation of a synchronous machine, which accounts for the inertia constant H_{GFr} and the damping factor D_{GFr}. In addition, a primary frequency control loop is included through a virtual droop coefficient R_V, providing frequency regulation capability analogous to the primary governor action in synchronous machines.

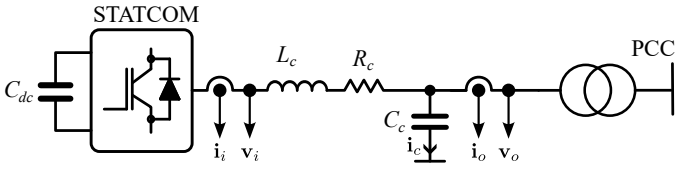


Fig. 3. STATCOM connected to the PCC.

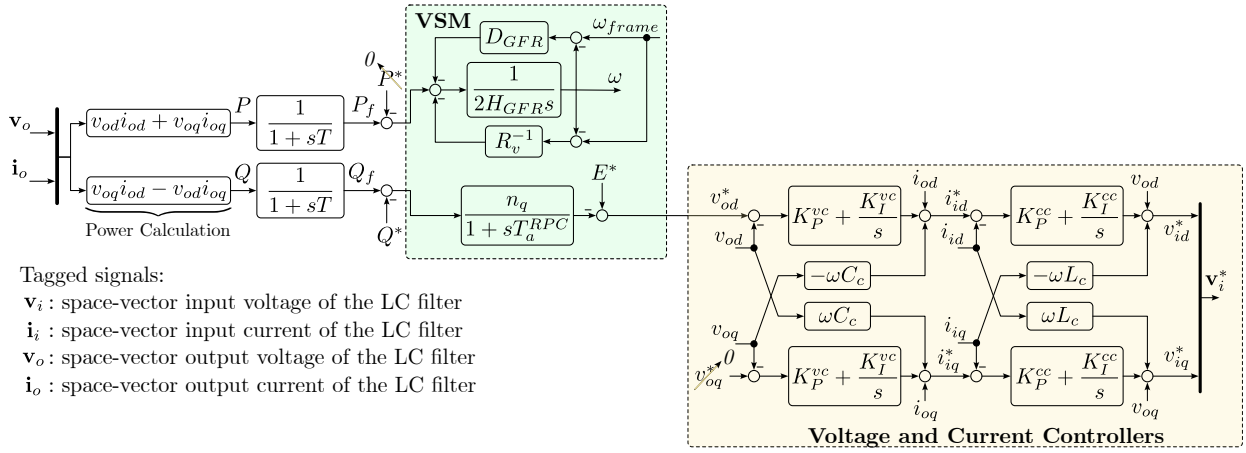


Fig. 4. Grid-forming STATCOM control block diagram.

TABLE I
GRID-FORMING STATCOM MODEL PARAMETERS

Parameter	Description	Value (pu)
C_{dc}	DC-link capacitance	0.10
L_c	LC filter inductance	0.20
R_c	LC filter resistance	0.02
C_c	filter capacitance	0.12
L_g	transformer inductance	0.1
R_g	transformer resistance	0.01
H_{GFr}	virtual inertia constant	6s
D_{GFr}	active power damping factor	0.1
R_v	virtual statism	3%
ω_e	base angular frequency	$2\pi 50$ rad/s
ω_{frame}	nominal angular frequency	1
n_q	reactive power droop gain	0.3
T_a^{RPC}	reactive power droop time constant	10ms
w_n	current control natural freq.	4000 rad/s
ζ	current control damping	0.707

Similarly, the voltage magnitude control in the GFr-STATCOM is implemented through a voltage vs reactive power droop mechanism. The droop gain n_q defines the voltage deviation as a function of the difference between the reference and measured reactive power, effectively reproducing the behavior of the excitation system in a synchronous machine. Moreover, a time constant T_a^{RPC} is introduced to emulate the dynamic response of an automatic voltage regulator (AVR) [26]. The voltage reference E^* represents the steady-state voltage magnitude imposed by the GFr STATCOM at the output of the LC filter prior to a reactive power disturbance, and its initial value is a result of a power-flow analysis.

The main parameters of the GFr STATCOM model are summarized in Table I. All values are expressed in per-unit (pu).

As illustrated in Fig. 4, the right-hand side of the block

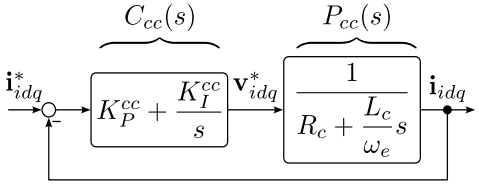


Fig. 5. Inner current-control loop block diagram.

diagram contains the "Voltage and Current Controller," which regulates the converter terminal variables. This block is organized in a cascaded structure with an inner current loop and an outer voltage loop. The inner loop ensures fast tracking of the converter currents, while the outer loop regulates the capacitor voltage according to the reference provided by the VSM. The design and tuning of these control loops are described in the following subsections.

1) Inner current control loop: The inner current loop is tuned using pole-placement as in [27]. The closed-loop block diagram is shown in Fig. 5.

The PI controller gains are given by (1)

$$K_I^{cc} = \frac{\omega_n^2 L_c}{\omega_e}, \qquad K_P^{cc} = \frac{2\zeta\omega_n L_c}{\omega_e} - R_c, \tag{1}$$

where ω_n and ζ are the desired natural frequency and damping ratio, L_c, R_c are the filter parameters and ω_e is the system base frequency.

2) Outer voltage control loop: Fig. 6 shows the outer voltage loop closed-loop block diagram, where the closed-loop current-control, $G_{cc} = i_{idq}/i_{idq}^*$, is considered part of the plant.

$$P_{vc}(s) = G_{cc}(s) \cdot \frac{\omega_e}{C_c \cdot s} \tag{2}$$

The controller (3) is tuned by phase margin design, with the objective of regulating the filter capacitor voltage.

$$C_{vc}(s) = K_P^{vc} + \frac{K_I^{vc}}{s} \tag{3}$$

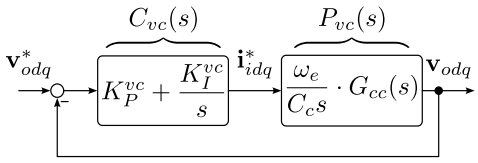


Fig. 6. Outer voltage-control loop block diagram.

The controller gains are obtained with the following procedure:

Algorithm 1 phase margin Based Voltage Controller Design

1: Select desired phase margin φ_m (e.g. $54°$).

2: Compute plant crossover frequency $\omega_{0,P}$ such that $\angle P_{vc}(j\omega_{0,P}) = -180° + \varphi_m$.

3: Set controller crossover: $\omega_{0,PI} = 0.8\,\omega_{0,P}$.

4: Evaluate the plant phase at the controller crossover: $\varphi_P = \angle P_{vc}(j\omega_{0,PI})$.

5: Compute the controller phase required to meet the desired margin: $\varphi_C = -180° + \varphi_m - \varphi_P$

6: Calculate the integral time constant (PI phase at $\omega_{0,PI}$): $T_I = \dfrac{\tan(\varphi_C + 90°)}{\omega_{0,PI}}$.

7: Obtain the plant gain $A_p = |P_{vc}(j\omega_{0,PI})|$

8: Set the controller gains: $K_P^{vc} = 1/A_p, \quad K_I^{vc} = K_P^{vc}/T_I$.

III. GFL-IBR PLL Stability Analysis

This section analyzes how the stability of the PLL in GFl-IBRs is affected under different system configurations. The study begins with the base case of an GFl-IBR (DFIG) connected alone to the grid, which serves as the reference scenario. Subsequently, the impact of adding a SC and a GFr STATCOM at the PCC is evaluated, followed by a comparison with the case of a GFl STATCOM. For each configuration, small-signal eigenvalue analysis and participation factors are used to identify the dominant modes influencing PLL dynamics. The analyses have been carried out using MATLAB/Simulink, supported by the VFlexP toolbox [28], which enables detailed modeling and eigenvalue-based stability assessment. This systematic approach allows quantifying the relative contribution of each compensating device to the enhancement of PLL stability.

A. Case 1: GFl-IBR (DFIG) alone

The SCR at the point of connection can be approximated using the base system quantities as discussed in [3], [29]:

$$SCR_{PCC} = \frac{1}{x_l}, \tag{4}$$

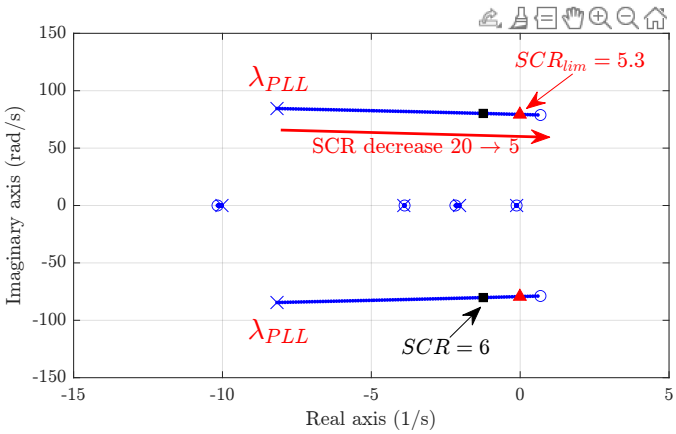


Fig. 7. Critical eigenvalue (λ_{PLL}) movement when SCR is decreased from 20 (cross) to 5 (circle) and the IBR is connected without a compensator device. The SCR limit at which the system becomes unstable is $SCR_{lim} = 5.3$ (triangle).

where x_l represents the per-unit reactance of the transmission line connecting the IBR to the infinite bus.

First, the critical SCR value at which the system becomes unstable is obtained. Fig. 7 illustrates the movement of the critical eigenvalue, λ_{PLL}, as the SCR decreases from 20 to 5, showing the degradation of stability when no compensating device is present. It was observed that instability arises when $SCR \approx 5.3$.

For all subsequent analyses, a nominal SCR of 6 is selected, which corresponds to a stable IBR operating close to the instability limit. Eigenvalue participation analysis, as defined in [30], shows that the most critical complex eigenvalue (see Table II) is the PLL control loop of the DFIG, λ_{PLL}, with the highest participation. This indicates that the PLL is the primary source of instability when the system approaches low SCR conditions as reported in [3], [23], [31]–[33].

TABLE II
Critical Complex Eigenvalue (λ_{PLL}) Participation Magnitudes

Variable Name	Magnitude
DFIG/θ_{PLL}	0.35
DFIG/V_{meas}^{PLL}	0.22
DFIG/ω_{PLL}	0.19
DFIG/V_{dc}	0.09
DFIG/xa_3	0.06
DFIG/ψ_s^d	0.02

B. Case 2: GFl-IBR (DFIG) with a SC

In this section, the impact of adding a SC on the PLL stability of the IBR is analyzed. The SCR is kept at 6, as defined in the previous section. As described in [3], the stability improvement is mainly due to the reduction of the impedance seen by the IBR. Specifically, the SC subtransient impedance, when connected in parallel with the line impedance, increases the system's effective short-circuit strength at the point of connection. For simplicity and to remain within the scope of this paper, the SC is considered without reactive power injection. The eigenvalue analysis shows that the critical complex

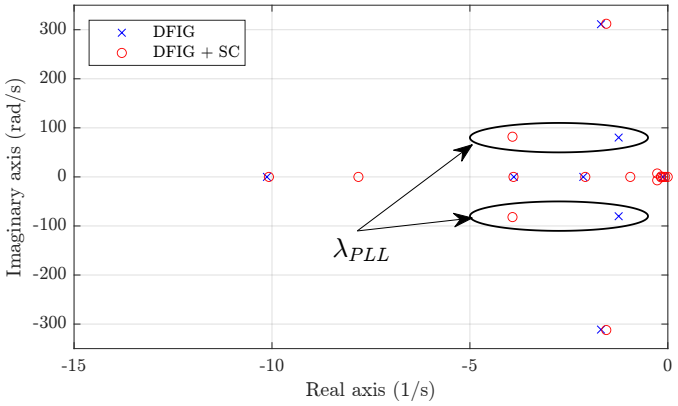


Fig. 8. Eigenvalues of a DFIG connected to an infinite grid with SCR = 6, with and without a SC.

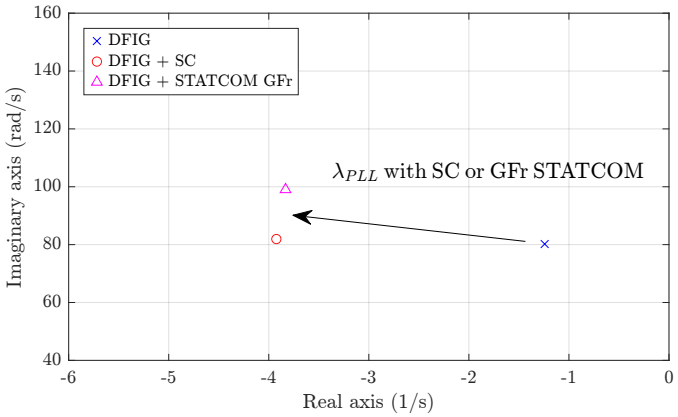


Fig. 9. Eigenvalue λ_{PLL} of a DFIG connected to an infinite grid with SCR = 6 alone, and with a SC and a GFr STATCOM with $\varphi_m = 54°$.

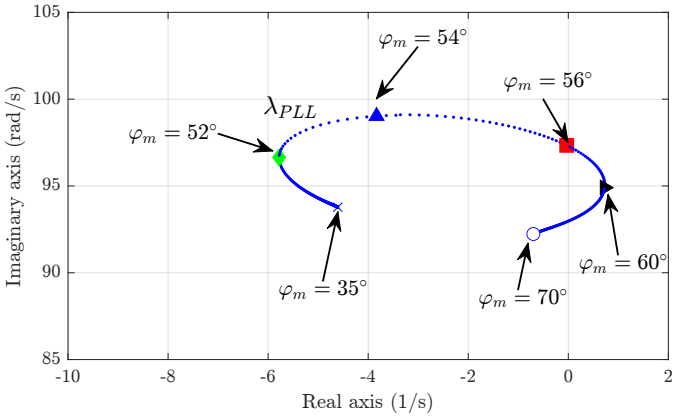


Fig. 10. Impact of the phase margin φ_m (from $\varphi_m = 35°$ (crosses) to $70°$ (circle) on the DFIG PLL control loop eigenvalues (λ_{PLL}) for a GFr STATCOM connected to a DFIG with an SCR = 6.

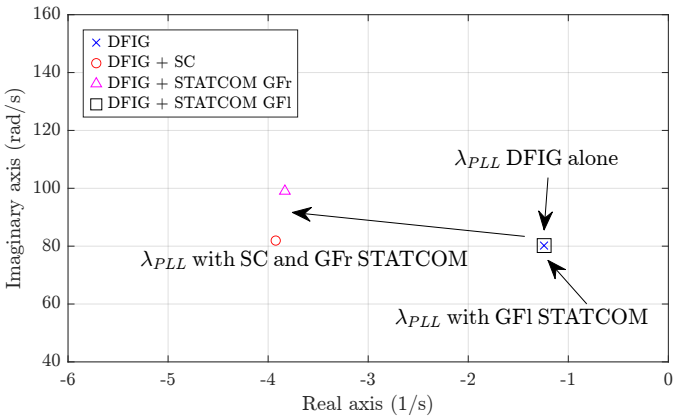


Fig. 11. Eigenvalue λ_{PLL} of a DFIG connected to an infinite grid with SCR = 6 with a SC, a GFr STATCOM, and a GFl STATCOM.

eigenvalues λ_{PLL}, which have the highest participation in the PLL control loop, have their real parts shifted further into the negative half-plane, indicating an increase in system stability.

The eigenvalue improvement can be visualized in Fig. 8, which shows that the real parts of the critical modes move further left in the complex plane, confirming the stabilization effect of the synchronous compensator.

C. Case 3: GFl-IBR (DFIG) with a GFr STATCOM

This section analyzes the impact of connecting a GFr STATCOM with phase margin $\varphi_m = 54°$ to the IBR system. The SCR is kept at 6, as defined in subsection Case 1. Fig. 9 illustrates the eigenvalue distribution.

The GFr STATCOM stabilizes the IBR PLL by imposing both voltage magnitude and frequency at its terminals. The speed of its voltage control loop, tuned using the phase margin design described in Algorithm 1, plays a crucial role: excessively fast or slow control can destabilize the IBR PLL. This effect is illustrated in Fig. 10, which shows eigenvalue variations for phase margins ranging from $\varphi_m = 35°$ to $70°$. The system becomes unstable (real part of $\lambda_{PLL} \geq 0$) with $57° \leq \varphi_m \leq 66°$.

D. Case 4: GFl-IBR (DFIG) with a GFl STATCOM

Finally, for comparison, a GFl STATCOM has also been analyzed. Fig. 11 shows the critical eigenvalue λ_{PLL} for all the four cases analysed: DFIG alone, with the SC, with the STATCOM in GFr mode and with the STATCOM in GFl mode. As expected, an STATCOM in GFl mode provides negligible improvement to the DFIG PLL stability, confirming the advantage of the grid-forming control strategy.

IV. Time-Domain Simulations

In order to complement the small-signal analysis, transient simulations have been performed for the different system configurations to evaluate the impact of compensating devices on GFl-IBR PLL stability under sudden disturbances.

A. Simulation Setup

The system models described in Section II are used for time-domain simulations. Four configurations are considered:

1) GFl-IBR alone (base case),
2) GFl-IBR with a SC,
3) GFl-IBR with a GFr STATCOM,
4) GFl-IBR with a GFl-STATCOM.

The transient response of the system is evaluated under a disturbance consisting of a 50 mHz pulse increase in the infinite-bus frequency, applied for 100 ms. The simulations are performed over a time horizon sufficient to observe the system's dynamic response, with a time step small enough to capture fast PLL dynamics.

The main variables analyzed are:

- Frequency at the buses where the IBR and compensating devices are connected.
- Rate of change of frequency (RoCoF) at the PCC, estimated using a windowed least-squares method [34].

B. Transient simulation results

The frequency perturbation induces a sudden mismatch between the grid frequency and the internal reference of the IBR PLL, allowing assessment of how effectively each compensating device mitigates the induced frequency excursion. The PLL-measured frequencies are presented in Fig. 12, where the results have been split into two comparisons for clarity.

Fig. 12(a) illustrates the response of the DFIG alone compared to the DFIG equipped with a GFl-STATCOM and the SC. It can be observed that the GFl-STATCOM provides negligible improvement over the base case, whereas the SC significantly mitigates the frequency transient. Subsequently, Fig. 12(b) focuses on the comparison between the two most effective solutions: the SC and the GFr-STATCOM.

A quantitative comparison is provided in Table III, which reports the maximum RoCoF, the frequency excursion at nadir, and its occurrence time for each configuration, alongside their relative variations with respect to the IBR-alone case.

The main observations are as follows:

- *IBR alone:* The base case exhibits the largest RoCoF = 0.405 Hz/s and the largest frequency excursion, Δf = 0.111 Hz, with the Nadir at 1.043 s.
- *IBR+GFl STATCOM:* The response is almost identical to the base case, with a RoCoF = 0.406 Hz/s (a negligible 0.25% increase in magnitude) and a Δf = 0.104 Hz at Nadir (a small reduction of 6.50% with respect to 0.111 Hz). This confirms that a GFl STATCOM provides almost no support to PLL synchronization stability.
- *IBR+SC:* The SC provides the largest improvement in frequency stability, reducing the RoCoF by 28.99% and improving the Δf (0.064 Hz) at Nadir by 42.09%, occurring at 1.041 s. Among all devices, the SC yields the most damped response and the smallest frequency excursion.
- *IBR+GFr STATCOM:* This configuration provides a moderate RoCoF reduction (22.5%), indicating partial mitigation of fast frequency excursions. Its influence on the Δf at Nadir is comparable to that of the SC (Δf = 0.075 Hz, i.e. -32.33%). The nadir occurs at 1.38 s, the latest among all devices.

These results demonstrate that SC and GFr STATCOMs effectively attenuate RoCoF and, in the case of SC, clearly help mitigate frequency deviations following a disturbance. In contrast, GFl STATCOMs provide almost no support, as their behavior remains governed by the same PLL that limits the IBR stability margin.

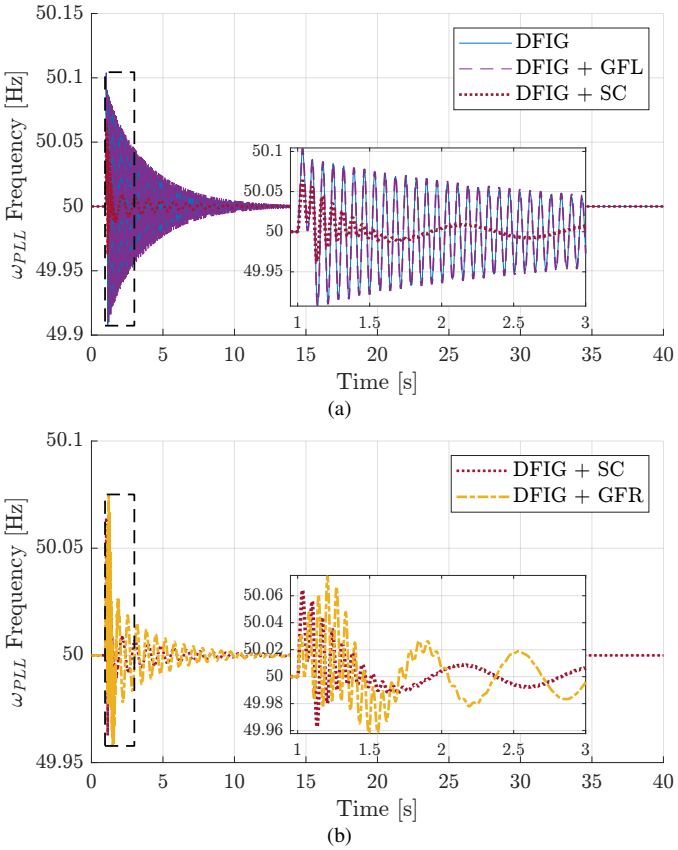


Fig. 12. PLL-measured frequency response of the IBR following a 50 mHz frequency pulse lasting 100 ms. (a) Comparison of DFIG alone, DFIG+GFl, and DFIG+SC. (b) Detailed comparison between DFIG+SC and DFIG+GFr.

V. Conclusions

This paper has analyzed the impact of SCs and GFr/GFl STATCOMs on the stability of the PLL in an IBR connected to a weak grid. In this work a DFIG is selected as the IBR due to its higher complexity compared to other IBRs. The following conclusions can be drawn:

- The base case with the IBR alone exhibits poor PLL stability under reduced SCR conditions. Eigenvalue analysis and transient simulations confirm that the system becomes unstable when the SCR falls below a certain value (SCR = 5.3 for the system in this paper).
- Adding a SC improves PLL stability by reducing the effective impedance seen from the IBR, thereby increasing the system SCR. This configuration achieves the lowest RoCoF and the lowest frequency excursion at nadir among all cases studied.
- A GFr STATCOM, although it does not increase SCR due to its limited fault current contribution, also enhances PLL stability. The mechanism is different: by imposing voltage and frequency at its terminals, the GFr STATCOM reduces the dynamic stress on the PLL.
- In contrast, a GFl STATCOM provides negligible improvement to PLL stability, with frequency dynamics nearly identical to the IBR-alone case.
- The design of the GFr STATCOM voltage controller using phase margin tuning has a clear effect on the

TABLE III
FREQUENCY STABILITY METRICS UNDER A 50 MHZ FREQUENCY PULSE APPLIED AT THE INFINITE BUS

Configuration	$\|\text{RoCoF}\|_{\max}$ [Hz/s]	$\Delta f_{\max}$ at Nadir [Hz]	Nadir Time [s]
IBR alone (base)	0.405	0.111	1.043
IBR + GFl STATCOM	0.406 (-0.25%)	0.104 (-6.50%)	1.042
IBR + SC	0.288 (-28.99%)	0.064 (-42.09%)	1.041
IBR + GFr STATCOM	0.314 (-22.5%)	0.075 (-32.4%)	1.380

stability of the PLL.

In summary, both SCs and GFr STATCOMs are effective in enhancing the stability of IBR PLLs, but through different mechanisms. SCs strengthen the grid by increasing SCR, while GFr STATCOMs provide voltage and frequency support directly. These findings suggest that GFr STATCOMs can serve as an alternative to SCs in scenarios where rotating machines are not available or desired. Future work will focus on extending the analysis to multi-machine systems, considering reactive power support from SCs, and exploring advanced tuning methods for GFr converters.

APPENDIX A
DOUBLY-FED INDUCTION GENERATOR MODEL

In this appendix, all the data related to the differential equations modeling the DFIG (taken from [27]) and the block diagrams of the control schemes used in this article (taken from [35]) are provided.

A. DFIG Electromagnetic Equations

In this appendix, the differential equations modeling the DFIG [27] and the control schemes block diagrams [35] are provided. By defining the space vectors $\mathbf{x}_k = [x_{kd}, x_{kq}]^T$ (for voltage v, current i, and flux ψ) where subscripts $k \in \{s, r\}$ denote stator and rotor respectively, the voltage equations are expressed as:

$$\begin{aligned} \mathbf{v}_s &= R_s \mathbf{i}_s + \frac{1}{\omega_0}\frac{d\boldsymbol{\psi}_s}{dt} + \omega_s \mathbf{J}\boldsymbol{\psi}_s \\ \mathbf{v}_r &= R_r \mathbf{i}_r + \frac{1}{\omega_0}\frac{d\boldsymbol{\psi}_r}{dt} + (\omega_s - \omega_r)\mathbf{J}\boldsymbol{\psi}_r \end{aligned} \tag{5}$$

where $\mathbf{J} = \begin{bmatrix} 0 & -1 \\ 1 & 0 \end{bmatrix}$ is the coupling matrix. R_s, R_r are resistances; $\omega_0, \omega_s, \omega_r$ are the base, synchronous, and rotor angular frequencies. The flux-current relations are given in matrix form by:

$$\begin{bmatrix} \boldsymbol{\psi}_s \\ \boldsymbol{\psi}_r \end{bmatrix} = \begin{bmatrix} L_s \mathbf{I}_2 & L_m \mathbf{I}_2 \\ L_m \mathbf{I}_2 & L_r \mathbf{I}_2 \end{bmatrix} \begin{bmatrix} \mathbf{i}_s \\ \mathbf{i}_r \end{bmatrix} \tag{6}$$

where $\mathbf{I}_2$ is a 2×2 identity matrix. The inductances are defined as $L_s = L_{\sigma s} + L_m$ and $L_r = L_{\sigma r} + L_m$, with $L_{\sigma s}, L_{\sigma r}$ being leakage inductances and L_m the mutual inductance.

Similarly, the GSC output filter dynamics are governed by:

$$\mathbf{v}_a = -R_a \mathbf{i}_a - \frac{1}{\omega_0}\frac{d\boldsymbol{\psi}_a}{dt} + \omega_s \mathbf{J}^T \boldsymbol{\psi}_a - \mathbf{v}_s \tag{7}$$

TABLE IV
DOUBLY FED INDUCTION GENERATOR PARAMETERS

Parameter	Description	Value [pu]
R_s, R_r	Stator, Rotor resistance	0.00734, 0.01225
$L_{\sigma s}, L_{\sigma r}$	Stator, Rotor leakage ind.	0.1178, 0.15349
L_m	Magnetizing inductance	4.709
H, c	Inertia (s), DC-link cap.	3.3, 0.0555
r_a, L_a	Filter resistance, inductance	0.1, 1
r_t, L_t	Transformer res., ind.	0.015, 0.15
c_f	Output filter capacitance	0.11
BW_{cc}, BW_{PLL}	Current, PLL bandwidth	1150rad/s, 8% BW_{cc}
BW_{PQ}	Outer power control bandwidth	5% BW_{cc}
K^{Te}_{opt}, ζ	Opt. torque gain, Damping	0.5896, $1/\sqrt{2}$

with the inductor flux defined as $\boldsymbol{\psi}_a = L_a \mathbf{i}_a$. Subscript a denotes the filter variables. The expanded version of these equations can be found in [3].

B. DFIG Electromechanical & Control Equations

The rotor swing equation and electrical torque T_e are defined as:

$$2H\omega_s \frac{d}{dt}\left(\frac{\omega_s - \omega_r}{\omega_s}\right) = T_m - T_e; \quad T_e = \boldsymbol{\psi}_r^T \mathbf{J}\mathbf{i}_r \tag{8}$$

where T_m is the mechanical torque and H the inertia constant.

C. DFIG rotor and grid side converter controllers

The controllers (taken from [35]) for the RSC and GSC are depicted in Fig. 13 and Fig. 14. The control logic operates in the stator-flux reference frame. The transformation from rotor dq-axes to this frame is:

$$\mathbf{x}_r^{\psi} = \mathbf{T}(\varphi)^{-1}\mathbf{x}_r; \quad \mathbf{T}(\varphi) = \begin{bmatrix} \cos\varphi & -\sin\varphi \\ \sin\varphi & \cos\varphi \end{bmatrix} \tag{9}$$

where the angle is $\varphi = \arctan(\psi_{sd}/\psi_{sq})$. The leakage factor is $\sigma = L_r - L_m^2/L_s$.

APPENDIX B
SYNCHRONOUS COMPENSATOR MODEL

This section details the SC model and its Automatic Voltage Regulator (AVR) [25].

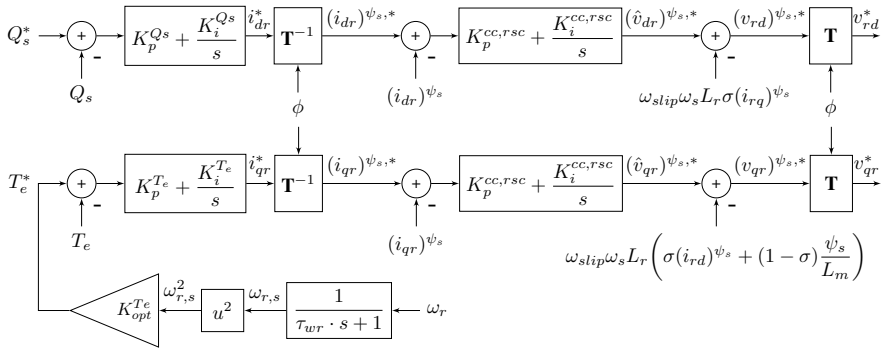


Fig. 13. Rotor side converter controllers block diagrams

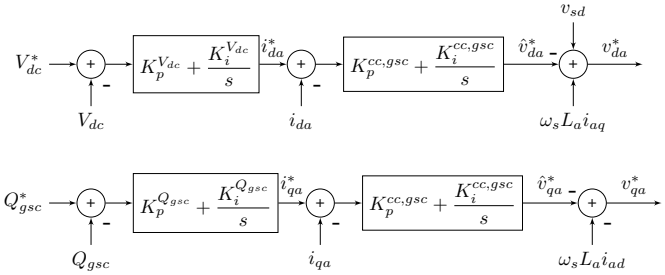


Fig. 14. Grid side converter controllers block diagrams

A. SC Electromagnetic & Electromechanical Equations

The per-unit stator voltage equations are given in vector form by:

$$\mathbf{v}_s = \frac{1}{\omega_0}\frac{d\boldsymbol{\psi}_s}{dt} + \omega_r \mathbf{J}\boldsymbol{\psi}_s - R_a \mathbf{i}_s \tag{10}$$

where $\mathbf{v}_s = [e_d, e_q]^T$, $\boldsymbol{\psi}_s = [\psi_d, \psi_q]^T$, $\mathbf{i}_s = [i_d, i_q]^T$, and $\mathbf{J}$ is the coupling matrix defined in the previous section.

The rotor circuit dynamics are defined by:

$$\mathbf{v}_r = \frac{1}{\omega_0}\frac{d\boldsymbol{\psi}_r}{dt} + \mathbf{R}_r \mathbf{i}_r \tag{11}$$

where the rotor vectors are $\mathbf{v}_r = [e_{fd}, 0, 0, 0]^T$, $\mathbf{i}_r = [i_{fd}, i_{1d}, i_{1q}, i_{2q}]^T$, and the resistance matrix is diagonal $\mathbf{R}_r = \text{diag}(R_{fd}, R_{1d}, R_{1q}, R_{2q})$.

The flux-current relationships are expressed in compact matrix form as:

$$\begin{bmatrix}\boldsymbol{\psi}_s \\ \boldsymbol{\psi}_r\end{bmatrix} = \begin{bmatrix}-\mathbf{L}_{ss} & \mathbf{L}_{sr} \\ -\mathbf{L}_{sr}^T & \mathbf{L}_{rr}\end{bmatrix}\begin{bmatrix}\mathbf{i}_s \\ \mathbf{i}_r\end{bmatrix} \tag{12}$$

where the inductance sub-matrices are explicitly defined as:

$$\begin{aligned}\mathbf{L}_{ss} &= \text{diag}(L_{ad} + L_l,\ L_{aq} + L_l) \\ \mathbf{L}_{rr} &= \begin{bmatrix} L_{ffd} & L_{fld} & 0 & 0 \\ L_{fld} & L_{11d} & 0 & 0 \\ 0 & 0 & L_{11q} & L_{aq} \\ 0 & 0 & L_{aq} & L_{22q}\end{bmatrix} \\ \mathbf{L}_{sr} &= \begin{bmatrix} L_{ad} & L_{ad} & 0 & 0 \\ 0 & 0 & L_{aq} & L_{aq}\end{bmatrix}\end{aligned} \tag{13}$$

Here, $\mathbf{L}_{ss}$ includes the stator leakage L_l and mutual inductances (L_{ad}, L_{aq}); $\mathbf{L}_{rr}$ contains the rotor self and mutual inductances (field winding f, and dampers $1d, 1q, 2q$); and $\mathbf{L}_{sr}$ represents the stator-rotor magnetic coupling. The electromechanical dynamics are governed by the swing equation:

$$2H\frac{d\omega_r}{dt} = T_m - T_e; \quad T_e = \boldsymbol{\psi}_s^T \mathbf{J}\mathbf{i}_s \tag{14}$$

where $T_m \approx 0$ for a SC (negligible losses).

The standard parameters (x_d, x'_d, T'_{d0}, etc.) relate to the fundamental parameters (L_{ad}, R_{fd}, etc.) through the classical transformations described in [25]. For the d-axis, key relations include $L_{fd} = L_{ad}(L'_d - L_{\sigma l})/(L_d - L'_d)$ and $T'_d = T'_{d0}(L'_d/L_d)$, with analogous expressions for the q-axis and damping windings. Note that since the base frequency equals the stator frequency, per-unit reactances equal per-unit inductances in Table V. The expanded version of this equations can be found in [3].

B. SC Automatic Voltage Regulator (AVR)

The AVR scheme adopted is shown in Fig. 15. The control parameters and the machine electrical data are listed in Table V.

REFERENCES

[1] R. H. Lasseter, Z. Chen, and D. Pattabiraman, "Grid-Forming Inverters: A Critical Asset for the Power Grid," *IEEE Journal of Emerging and Selected Topics in Power Electronics*, vol. 8, no. 2, pp. 925–935, Jun. 2020.

[2] S. D'Arco and J. A. Suul, "Equivalence of Virtual Synchronous Machines and Frequency-Droops for Converter-Based MicroGrids," *IEEE Transactions on Smart Grid*, vol. 5, no. 1, pp. 394–395, Jan. 2014.

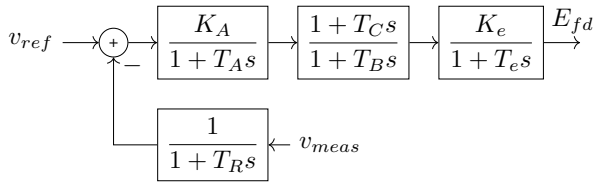


Fig. 15. Automatic voltage regulator used

TABLE V
SYNCHRONOUS COMPENSATOR PARAMETERS

Parameter	Description	Value [pu]
	General & Stator	
$R_s, x_{\sigma l}$	Stator res., Leakage ind.	0.018, 0.1
H, D	Inertia (s), Friction coeff.	8.2, 0.01
$r_{\sigma fd}$	Excitation leakage res.	$5.2 \cdot 10^{-4}$
	Reactances (Unsaturated / Saturated)	
x_d, x_d^s	d-axis synchronous	1.6 / 1.5
x_q, x_q^s	q-axis synchronous	0.66 / 0.62
$x'_d, x_d^{'s}$	d-axis transient	0.23 / 0.20
$x''_d, x_d^{''s}$	d-axis subtransient	0.15 / 0.13
$x''_q, x_q^{''s}$	q-axis subtransient	0.22 / 0.2
	Time Constants [s]	
T'_d, T'_{d0}	d-axis transient (Short/Open)	1.3, 10
T''_d, T''_{d0}	d-axis subtransient (Short/Open)	0.03, 0.04
T'_q, T'_{q0}	q-axis transient (Short/Open)	1.1, 15
T''_q	q-axis subtransient	0.15
	AVR Parameters	
K_A, T_A	Main regulator Gain, Delay	200, 10 ms
T_C, T_B	Washout filter (Num/Den)	1, 12
K_E, T_E	Diode bridge Gain, Delay	1, 1.15 s
T_R	Measure filter delay	10 ms

[3] J. Suárez-Porras, F. Fernández-Bernal, L. Rouco, and A. Tomás-Martín, "Synchronous Compensators Considering Reactive Power for PLL Stability Improvement and Short-Circuit Ratio Evaluation," *IEEE Transactions on Energy Conversion*, pp. 1–17, 2025.

[4] M. Caldora, L. Cantoni, M. C. Falvo, A. Coretti, A. Lazzarin, C. Vergine, A. Cinque, and B. Aluisio, "Synchronous condensers with flywheel for power systems with high penetration of RES: The case of Italian transmission grid," in *2022 AEIT International Annual Conference (AEIT)*, Oct. 2022, pp. 1–5.

[5] M. Khan, W. Wu, and L. Li, "Grid-forming control for inverter-based resources in power systems: A review on its operation, system stability, and prospective," *IET Renewable Power Generation*, vol. 18, no. 6, pp. 887–907, 2024.

[6] C. Yang, L. Huang, H. Xin, and P. Ju, "Placing Grid-Forming Converters to Enhance Small Signal Stability of PLL-Integrated Power Systems," *IEEE Transactions on Power Systems*, vol. 36, no. 4, pp. 3563–3573, Jul. 2021.

[7] A. Aamir, L. Qiao, C. Guo, A. U. Rehman, and Z. Yang, "Impact of synchronous condenser on the dynamic behavior of LCC-based UHVDC system hierarchically connected to AC system," *CSEE Journal of Power and Energy Systems*, vol. 5, no. 2, pp. 190–198, Jun. 2019.

[8] V. Arayamparambil Vinaya Mohanan, I. M. Mareels, R. J. Evans, and R. R. Kolluri, "Stabilising influence of a synchronous condenser in low inertia networks," *IET Generation, Transmission & Distribution*, vol. 14, no. 17, pp. 3582–3593, 2020.

[9] A. González-Cajigas, J. Roldán-Pérez, and E. J. Bueno, "Design and Analysis of Parallel-Connected Grid-Forming Virtual Synchronous Machines for Island and Grid-Connected Applications," *IEEE Transactions on Power Electronics*, vol. 37, no. 5, pp. 5107–5121, May 2022.

[10] C. Henderson, A. Egea-Alvarez, T. Kneuppel, G. Yang, and L. Xu, "Grid Strength Impedance Metric: An Alternative to SCR for Evaluating System Strength in Converter Dominated Systems," *IEEE Transactions on Power Delivery*, vol. 39, no. 1, pp. 386–396, Feb. 2024.

[11] D. B. Rathnayake, M. Akrami, C. Phurailatpam, S. P. Me, S. Hadavi, G. Jayasinghe, S. Zabihi, and B. Bahrani, "Grid Forming Inverter Modeling, Control, and Applications," *IEEE Access*, vol. 9, pp. 114 781–114 807, 2021.

[12] W. Tang, W. Zheng, B. Zhou, Z. Yang, and Y. Zhang, "Transient Stability Analysis Between Grid-Following DFIG-WT and Grid-Forming Converter in Electromechanical Timescale," *IEEE Transactions on Energy Conversion*, pp. 1–10, 2024.

[13] J. Liu, W. Yao, J. Wen, J. Fang, L. Jiang, H. He, and S. Cheng, "Impact of Power Grid Strength and PLL Parameters on Stability of Grid-Connected DFIG Wind Farm," *IEEE Transactions on Sustainable Energy*, vol. 11, no. 1, pp. 545–557, Jan. 2020.

[14] D. Dong, B. Wen, D. Boroyevich, P. Mattavelli, and Y. Xue, "Analysis of Phase-Locked Loop Low-Frequency Stability in Three-Phase Grid-Connected Power Converters Considering Impedance Interactions," *IEEE Transactions on Industrial Electronics*, vol. 62, no. 1, pp. 310–321, Jan. 2015.

[15] J. Hu, Q. Hu, B. Wang, H. Tang, and Y. Chi, "Small Signal Instability of PLL-Synchronized Type-4 Wind Turbines Connected to High-Impedance AC Grid During LVRT," *IEEE Transactions on Energy Conversion*, vol. 31, no. 4, pp. 1676–1687, Dec. 2016.

[16] J. Geis-Schroer, A. R. Nair, S. Patel, and S. Kamalasadan, "Modeling and Analysis of Weak Grid Considering Phase Locked Loop and Synchronous Condenser Effect on Grid Stability," in *2020 IEEE International Conference on Power Electronics, Smart Grid and Renewable Energy (PESGRE2020)*, Jan. 2020, pp. 1–6.

[17] Y. Wang, L. Wang, and Q. Jiang, "Impact of Synchronous Condenser on Sub/Super-Synchronous Oscillations in Wind Farms," *IEEE Transactions on Power Delivery*, vol. 36, no. 4, pp. 2075–2084, Aug. 2021.

[18] T. Prevost, G. Denis, and C. Coujard, "Future grid stability, a cost comparison of Grid-Forming and Synchronous Condenser based solutions," in *2020 22nd European Conference on Power Electronics and Applications (EPE'20 ECCE Europe)*, Sep. 2020, pp. P.1–P.9.

[19] D. Lepour, M. Paolone, G. Denis, C. Cardozo, T. Prevost, and E. Guiu, "Performance assessment of Synchronous Condensers vs Voltage Source Converters providing grid-forming functions," in *2021 IEEE Madrid PowerTech*, Jun. 2021, pp. 1–6.

[20] T. Qoria, F. Gruson, F. Colas, X. Guillaud, M.-S. Debry, and T. Prevost, "Tuning of Cascaded Controllers for Robust Grid-Forming Voltage Source Converter," in *2018 Power Systems Computation Conference (PSCC)*, Jun. 2018, pp. 1–7.

[21] H. Wu and X. Wang, "Small-Signal Modeling and Controller Parameters Tuning of Grid-Forming VSCs With Adaptive Virtual Impedance-Based Current Limitation," *IEEE Transactions on Power Electronics*, vol. 37, no. 6, pp. 7185–7199, Jun. 2022.

[22] "IEEE Guide for Planning DC Links Terminating at AC Locations Having Low Short-Circuit Capacities," *IEEE Std 1204-1997*, pp. 1–216, Jan. 1997.

[23] J. Z. Zhou, H. Ding, S. Fan, Y. Zhang, and A. M. Gole, "Impact of Short-Circuit Ratio and Phase-Locked-Loop Parameters on the Small-Signal Behavior of a VSC-HVDC Converter," *IEEE Transactions on Power Delivery*, vol. 29, no. 5, pp. 2287–2296, Oct. 2014.

[24] G. Abad, J. Lopez, M. Rodriguez, L. Marroyo, and G. Iwanski, *Doubly Fed Induction Machine: Modeling and Control for Wind Energy Generation*, ser. IEEE Press Series on Power and Energy Systems. Wiley, 2011.

[25] P. Kundur, N. Balu, and M. Lauby, *Power System Stability and Control*, ser. EPRI Power System Engineering Series. McGraw-Hill Education, 1994.

[26] S. D'Arco, J. A. Suul, and O. B. Fosso, "A Virtual Synchronous Machine implementation for distributed control of power converters in SmartGrids," *Electric Power Systems Research*, vol. 122, pp. 180–197, May 2015.

[27] L. Rouco and J. Zamora, "Dynamic patterns and model order reduction in small-signal models of doubly fed induction generators for wind power applications," in *2006 IEEE Power Engineering Society General Meeting*. Montreal, Que., Canada: IEEE, 2006, p. 8 pp.

[28] A. Tomás-Martín, C. D. Zuluaga-Ríos, J. Suárez-Porras, B. Kazemtabrizi, J. García-Aguilar, L. Sigrist, and A. García-Cerrada, "A vector-based flexible-complexity tool for simulation and small-signal analysis of hybrid AC/DC power systems," *Sustainable Energy, Grids and Networks*, vol. 43, p. 101817, Sep. 2025.

[29] "IEEE Guide for Planning DC Links Terminating at AC Locations Having Low Short-Circuit Capacities," *IEEE Std 1204-1997*, pp. 1–216, Jan. 1997.

[30] I. J. Perez-arriaga, G. C. Verghese, and F. C. Schweppe, "Selective Modal Analysis with Applications to Electric Power Systems, PART I: Heuristic Introduction," *IEEE Transactions on Power Apparatus and Systems*, vol. PAS-101, no. 9, pp. 3117–3125, Sep. 1982.

[31] W. Dong, H. Xin, D. Wu, and L. Huang, "Small Signal Stability Analysis of Multi-Infeed Power Electronic Systems Based on Grid Strength Assessment," *IEEE Transactions on Power Systems*, vol. 34, no. 2, pp. 1393–1403, Mar. 2019.

[32] C. Guo, C. Zhao, R. Iravani, H. Ding, and X. Wang, "Impact of phase-locked loop on small-signal dynamics of the line commutated converter-based high-voltage direct-current station," *IET Generation, Transmission & Distribution*, vol. 11, no. 5, pp. 1311–1318, 2017.

[33] T. Gu, P. Wang, D. Liu, A. Sun, D. Yang, and G. Yan, "Modeling and small-signal stability analysis of doubly-fed induction generator integrated system," *Global Energy Interconnection*, vol. 6, no. 4, pp. 438–449, Aug. 2023.

[34] H. Yin, Y. Wu, W. Qiu, C. Zeng, S. You, J. Tan, A. Hoke, C. J. Kruse, B. W. Rockwell, K. A. Kawamura, and Y. Liu, "Precise ROCOF estimation algorithm for low inertia power grids," *Electric Power Systems Research*, vol. 209, p. 107968, Aug. 2022.

[35] F. Mei and B. C. Pal, "Modelling of doubly-fed induction generator for power system stability study," in *2008 IEEE Power and Energy Society General Meeting - Conversion and Delivery of Electrical Energy in the 21st Century*. Pittsburgh, PA, USA: IEEE, Jul. 2008, pp. 1–8.